THE JOURNAL OF PHYSICAL CHEMISTRY C
A JOURNAL OF THE AMERICAN CHEMICAL SOCIETY

pubs.acs.org/JPCC

Article

Naphtho[2,3-*a*]pyrene Thin Films – H, I, or J? Aggregate Alphabet Soup Served over Triplet Pair States

Colette M. Sullivan, Adrienn M. Szucs, Theo Siegrist, and Lea Nienhaus*

Cite This: *J. Phys. Chem. C* 2024, 128, 19248–19259

Read Online

ACCESS | Metrics & More | Article Recommendations | Supporting Information

ABSTRACT: Photon upconversion in the solid state has the potential to improve existing solar and infrared imaging technologies due to its achievable efficiency at low power thresholds. However, despite considerable advancements in solution-phase upconversion, expanding the library of potential solid-state annihilators and developing a fundamental understanding of their solid-state behaviors remains challenging due to intermolecular coupling affecting the underlying energy landscape. Naphtho[2,3-*a*]pyrene has shown promise as a suitable solid-state annihilator. However, the origin of its multiple underlying emissive features remains unknown. To this point, here, we investigate NaPy/poly(methyl methacrylate) thin films at varying concentrations to tune the intermolecular coupling strength to determine its photophysical properties at a range of temperatures between 300–50 K. The results suggest that the multiple emissive features present in the NaPy thin film emission at room temperature arise from a multidimensional I-aggregate (520 nm), an excimer (550 nm), and a strongly coupled J-dimer (620 nm). In addition, we find that at low temperatures, the emission spectrum is dominated by direct emission from the ^{1}(TT) state.

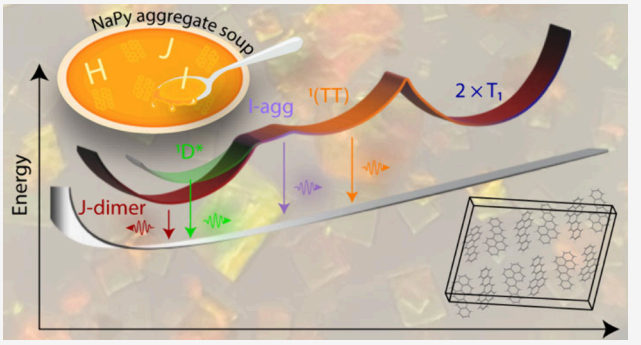

INTRODUCTION

Solid-state infrared-to-visible upconversion (UC) bears promise in applications including solar energy, anticounterfeiting and infrared sensing and imaging.[1−5] Triplet−triplet annihilation upconversion (TTA-UC) is particularly promising for low-light applications since it can become efficient at low light intensities. Due to the low direct absorption cross sections of spin-triplet states, upconversion systems consist of two parts: the triplet sensitizer and the annihilator.[6−14] In the case of perovskite-sensitized upconversion, the perovskite sensitizes the triplet state of the annihilator by charge transfer, akin to an in situ upconversion light emitting diode.[15−18] While absorbance up to 60% of the incident near-infrared light in the perovskite sensitizer has been achieved,[19] the annihilator library must be expanded and quantum yields improved. Currently, rubrene, the 'drosophila of upconversion' is the most commonly utilized annihilator in solid-state devices.[18,20−25] However, the inherent ∼0.4 eV energy loss during triplet sensitization of rubrene limits the achievable apparent anti-Stokes shift when using perovskite sensitizers.[19] Hence, recent efforts have been focused on finding new annihilators to increase the energy of the emitted light.[26−28]

We have recently introduced naphtho[2,3-*a*]pyrene (NaPy) as a viable annihilator for perovskite-sensitized TTA-UC.[28] To date, the photophysical properties of NaPy have not been well explored. Since both tetracene and pyrene backbone moieties are present, it is a molecule with possibly rich photophysical properties, particularly with respect to solid-state applications.

Interesting results have been observed via scanning tunneling microscopy, where NaPy was shown to self-assemble on gold surfaces in chiral domains.[29,30] In addition, one study has suggested that NaPy forms an unusual nonemissive J-aggregate.[31] As our previous results indicate emission from the excited state of NaPy in all forms - from isolated molecules in solution to thin films and ordered single crystals - a deeper dive into the underlying photophysical properties of NaPy is required to unravel the nature of the emissive state. In addition, our previous study indicated the presence of multiple emissive states which we had simply referred to as S_1' and S_1'' due to their unknown underlying nature.[28] The ratio of these two emissive states differed based on the degree of underlying crystallinity: "amorphous", crystallite, and single crystal. However, to date, the nature of these emissive states has not yet been investigated in detail.

Received: August 23, 2024
Revised: October 24, 2024
Accepted: October 28, 2024
Published: November 5, 2024

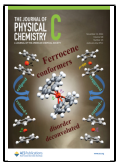

https://doi.org/10.1021/acs.jpcc.4c05675
J. Phys. Chem. C 2024, 128, 19248–19259

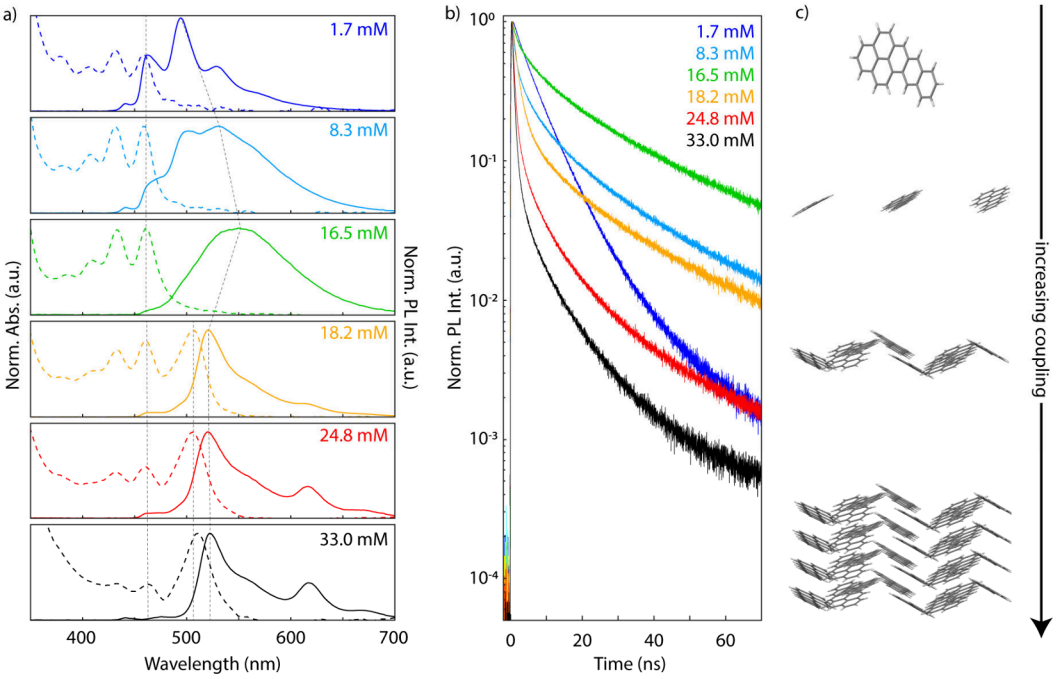

Figure 1. a) Normalized absorption and b) fluorescence spectra for the different NaPy/PMMA thin films collected under 405 nm excitation. The gray dotted lines are included as guides to the eye. c) Fluorescence decays for the NaPy/PMMA films collected under 405 nm pulsed excitation (1 MHz, 64.9 mW cm^{-2}). c) Schematic of the increased NaPy concentration resulting in a smaller intermolecular distance and increased coupling and ordered molecular packing.

Polyacenes have rich photophysical properties, particularly upon condensation into the solid state, where the intimate interactions can result shifts in the absorption/emission properties, induce singlet fission or cause aggregation-related effects.[32−35] In polyacene thin films, the originally planar acene backbones can be present in twisted or planar confirmations depending upon the underlying molecular arrangement, resulting in variations of the triplet T_1 and singlet S_1 energy manifolds, which in turn can influence recombination rates, rates of singlet fission and triplet−triplet annihilation. Furthermore, disorder can result in symmetry breaking, facilitating effects like singlet fission or TTA-UC.[36−39] Electronic coupling between adjacent molecules in aggregates is also known to impact the optical transitions. Using the point-dipole approximation, the Coulomb coupling V between two transition dipole moments $\vec{\mu}$ is described as

$$V = \frac{\mu^2(1 - 3\cos^2\theta)}{4\pi\varepsilon R^3} \quad (1)$$

Where θ is the angle between the transition dipole moments and the center-to-center vector $\vec{R}$ and R describes the distance between dipoles (the magnitude of the vector $\vec{R}$). If the coupling term is negative, this is referred to as J-type aggregation, while positive coupling results in H-aggregates.[40−43] H-type aggregation causes a hypsochromic shift, while J-type aggregation results in a bathochromic shift of the absorption spectrum.[35,44] In addition, H-type aggregation commonly suppresses emission, while J-aggregates generally feature superradiant emission with a low Stokes shift, high quantum yields, and fast radiative recombination rates.[44−46]

However, while conventional H- and J-aggregate theory sufficiently describes one-dimensional aggregate structures, the strict distinction can fail in multidimensional aggregates, as both H- and J-type coupling (considering both in-plane and out-of-plane coupling) can be present simultaneously leading to the HJ aggregate characterization by Spano and co-workers.[45,47] The herringbone nature of the crystal structure of many solid polyacenes requires additional factors to be considered, leading to detailed investigations of HB aggregates in literaure.[45,48,49] In addition to the extensive studies by Spano, Caram and co-workers have more recently introduced the term I-aggregate to describe a two-dimensional aggregate where long-range coupling is J-type ($V_{LR} < 0$) due to the in-plane transition dipole, while the short-range coupling V_{SR} is positive.[34] However, the magnitude of the positive coupling is smaller than that of the negative coupling, leading to an overall net negative coupling and bathochromic shift of the absorption of the aggregate.

Beyond H-, I-, and J-type coupling between monomers, excimer formation is also possible. In contrast to aggregation-based effects which influence both the electronic ground state and excited state, the excited state dimer, or excimer, only exists within the excited state.[50,51] Excimer $^1D^*$ formation and subsequent relaxation can be described by the following kinetic model:

$$^1M^* + {}^1M \leftrightharpoons {}^1D^* \quad (2)$$

$$^1D^* \rightarrow {}^1M + {}^1M + h\nu_D \quad (3)$$

Where $^1M^*$ and ^1M are the excited and ground state monomer, respectively. The ground state is dissociative; hence, the steady-state absorption spectrum is not influenced by excimer formation. However, the emission is shifted to lower energies than the monomer and is commonly broad and featureless.[52,53] The exact molecular structure of an excimer state is not commonly known but is often depicted as a pair of aligned molecules. A special type of excimer is a strongly

https://doi.org/10.1021/acs.jpcc.4c05675
J. Phys. Chem. C 2024, 128, 19248−19259

coupled localized excited state H- or J-type dimer, leading to considerable shifts in energy.[54,55]

To understand the role of aggregation, dimer formation, and monomer emission in NaPy and unravel the underlying photophysics of the molecule in different local environments, we here investigate how the properties of NaPy change when going from the isolated molecule in solution to the ordered molecular structure in the single crystal. NaPy is a particularly interesting molecule for such photophysical studies, as it unlike many common tetracene or anthracene derivatives does not have rotational symmetry or an intramolecular mirror plane. In the P21/c space group NaPy assembles in a "head-to-tail" herringbone structure, where adjacent molecules in the unit cell alternate orientation.

To minimize the possible side effects of undesired aggregation at low concentrations upon fabrication of thin films, we utilize a poly(methyl methacrylate) (PMMA) matrix to ensure spacing between individual molecules at low concentrations, essentially mimicking the solution properties. By increasing the NaPy loading in the PMMA matrix, we can systematically reduce the average intermolecular spacing and investigate the impact of NaPy concentration and the resulting intermolecular coupling on the photophysical properties as described in Figure 1.

Our results indicate that the multiple emissive states present in previously investigated NaPy thin films at room temperature stem from the aggregate at 520 nm, the excimer at 550 nm and a strongly coupled red-shifted J-dimer (J-coupled excimer) at 620 nm, which acts similar to a trap state. At low temperatures, the dominant emissive feature is the correlated triplet pair state ^{1}(TT) generated by singlet fission, as the ambient thermal energy is not sufficient to form uncorrelated triplet states.

MATERIALS AND METHODS

Device Synthesis. Glass substrates were cleaned via sonication for 15 min in each of the respective solutions: 2% Hellmanex, deionized water, isopropanol and acetone. Following sonication, the substrates were treated with UV-ozone.

Naphtho[2,3-*a*]pyrene (NaPy > 98%, TCI) and poly(methyl methacrylate) (PMMA, Sigma) were used without further purification. Stock solutions of 10 mg/mL of NaPy in anhydrous toluene (Sigma) and a 3% *w*/*w* PMMA solution in anhydrous toluene (Sigma) were prepared. The different concentrations of NaPy/PMMA thin films were prepared through appropriate dilutions, then spin coated at 6000 rpm. Films were encapsulated with a coverslip using a two-part epoxy (Devcon) under an inert nitrogen atmosphere (<0.5 ppm of O_2) prior to removal from the glovebox.

Films for the temperature dependent X-ray diffraction measurements were prepared as described and drop cast onto sapphire substrates to minimize background scattering.

Temperature Control. Temperature control for all steady-state and time-resolved emission experiments were collected using a He-filled cryocooler (Air Products). The encapsulated films were mounted onto a coldfinger optical sample mount prior to sheath evacuation (~10^{-5} mBar). A PID Digital Temperature Controller Model 9650 (Scientific Instruments) was used to maintain the desired temperature. The coldfinger was left to equilibrate for approximately 1 min prior to collecting absorbance and fluorescence spectra for each temperature point.

Steady-State Absorption Spectroscopy. A Thermo Scientific Evolution 220 Spectrophotometer was used for all absorption spectra.

Steady-State Emission Spectroscopy. Direct excitation emission spectra were collected with a 405 nm continuous wave laser (LDH-D-C-405, PicoQuant) at a power density of 30 W cm^{-2} for the room temperature NaPy/PMMA measurements and 3 W cm^{-2} for the temperature-dependent measurements. A 425 nm long-pass filter (Chroma Tech) to remove excess laser scattering. An Ocean Insight emission spectrometer (HR2000+ES) was used to collect all spectra.

Time-Resolved Emission Spectroscopy. NaPy fluorescence decays were measured through time-correlated single photon counting (TCSPC) with a 405 nm picosecond pulsed laser (LDH-D-C-405, PicoQuant) with a 1 MHz repetition frequency at a power density of 64.9 mW cm^{-2} for the room temperature spectra and 67 mW cm^{-2} for the temperature dependent measurements. A 425 nm long-pass filter (Chroma Tech) was used to remove laser scatter. To isolate the underlying spectral features, a 500 nm short pass (Thorlabs), 550 nm long pass (Thorlabs), 550 nm bandpass (fwhm = 40 nm, Thorlabs), and 635 nm bandpass (fwhm = 10 nm, Thorlabs) filters were used. A HydraHarp 400 event timer (PicoQuant) connected to a single-photon avalanche photodiode (Micro Photon Devices) was used to collect photon arrival times for all measurements. Laser powers were measured with a silicon power meter (PM100-D, Thorlabs), and spot sizes were calculated using the razor blade method (90:10).

Single Crystal Diffraction. Single crystal diffraction was carried out using a STOE Stadivari 4-circle diffractometer equipped with a Dectris Eiger detector and an Oxford Cryostream 1000. The measurement temperature was 150 K. The data collection used the X-Area program suite [reference X-Area Single Crystals Diffraction Software, Version 2.1, STOE & Cie GmbH, Darmstadt (2022)], and the refinements used the program suite CRYSTALS.[56]

Powder X-ray Diffraction. X-ray powder patterns were acquired using an Anton Paar XRDynamic 500 powder diffractometer equipped with the CHC Plus+ Cryo & Humidity Chamber and a Bragg−Brentano monochromator. The diffractometer was configured with liquid nitrogen cooling and operated under vacuum conditions. The cooling rate was maintained at 20 K per minute. Powder pattern measurements were taken at ambient temperature (298 K), 273 K, 223 K, 173 K, 123 K, and 110 K and once again at ambient temperature following the lowest temperature scan. The measurements were performed with Cu Kα radiation, using a step size of 0.01° from 5 to 40° 2θ at 200.691 s per step.

Scanning Electron Microscopy. Samples were platinum-coated (3 nm) prior to analysis. High-resolution imaging was conducted using a Tescan MIRA 4 field emission scanning electron microscope (FE SEM). Imaging was performed with secondary electrons (SE) and in-beam SE detectors at an accelerating voltage of 5 kV.

RESULTS AND DISCUSSION

Figure 1a shows the absorption and emission spectra of thin films spin coated from a 1.7−24.8 mM solution of NaPy in a PMMA matrix and a spin coated thin film of the stock NaPy solution (33.0 mM). As expected, the spectra at low concentration show a slight redshift of the 0−0 vibronic feature at ~460 nm, caused by increasing intermolecular

https://doi.org/10.1021/acs.jpcc.4c05675
J. Phys. Chem. C 2024, 128, 19248−19259

coupling due to a smaller average intermolecular distance due to the increased concentration. More interestingly, an additional red-shifted absorption feature with strong oscillator strength appears for the three highest concentrations 18.2−33.0 mM, indicating J-type or I-type aggregation.[34,45,57] A clear change in the dominant emissive state is found as the concentration is increased. For the lowest concentration (monomer-like) we find the expected vibronic progression with ν = 0.17 eV, resulting in emission features at 463, 494, 528, and 570 nm. In addition, a small, blue-shifted feature appears at 441 nm, assigned to H-band emission. Interestingly, despite negligible changes in the absorption spectrum, the emission spectrum changes greatly when increasing the NaPy concentration to 8.3 mM NaPy/PMMA. The vibronic progression becomes much less distinct, and the spectrum significantly broadens (vide supra). Further increase of the concentration to 16.5 mM NaPy/PMMA results in a broad featureless emission spectrum. In agreement with the unaltered absorption spectrum at this concentration corresponding to the ground state, this broad emission can be attributed to the NaPy excimer which exists only within the excited state. A minor increase of the concentration from 16.5 to 18.2 mM NaPy/PMMA causes another drastic change to the emission spectrum. The emission narrows and blueshifts, resulting in a small Stokes shift of 0.07 eV, as predicted for J-type aggregation. In addition, a small shoulder is present at ∼560 nm, the previously determined excimer emission wavelength. Upon further increasing the NaPy concentration to 24.8 and 33.0 mM, growth of an additional red-shifted emission feature at 620 nm with an apparent vibronic progression at ∼670 nm (ν = 0.15 eV) is observed. This is in agreement with our previous result, where we observed an increase in the red-shifted emission at 620 when going from a spin-coated thin film to a microcrystalline film and a single crystal: with increasing crystallinity and increasing aggregate absorption feature, the feature at 620 nm increases in intensity.[28] The emission intensity normalized to the absorbance at the excitation wavelength of 405 nm is shown in the Supporting Information Figure S1.

The corresponding fluorescence decay dynamics are shown in Figure 1b. To capture the rich dynamics of the disordered system and facilitate direct comparison, the decay dynamics are fit to triexponential decays unless otherwise noted.

$$I(t) = A_1\exp\left(-\frac{t}{\tau_1}\right) + A_2\exp\left(-\frac{t}{\tau_2}\right) + A_3\exp\left(-\frac{t}{\tau_3}\right) \quad (4)$$

The extracted amplitude-weighted average lifetimes $\tau_{ave} = \frac{\sum_i A_i\tau_i}{\sum_i A_i}$ for these samples are tabulated in Table 1 (Table S1). An interesting trend is found: the decay for the lowest NaPy concentration, which is "monomer-like" appears nearly monoexponential. As the concentration is increased, the early time decay rate increases, possibly due to intermolecular energy transfer between the emissive states. As the fraction of excimer emission is increased, the fluorescence decay dynamics become more multiexponential and the lifetime elongates, with the longest lifetime correlated to the pure excimer emission. Further increase in NaPy concentration results in a concurrent shortening of the lifetime, as expected due to the fast recombination rates expected in J-coupled aggregates, with the fastest lifetime correlated to the 33.0 mM spin-coated NaPy film (compare Figure 1b). A schematic of the impact of the increasing concentration on the molecular arrangement is shown in Figure 1c.

Table 1. Amplitude-Weighted Average Lifetimes for the NaPy/PMMA Thin Films Depicted in Figure 1 Based on a Triexponential Fit

Concentration/mM	τ_{ave}/ns
1.7	6.3
8.3	4.8[a]
16.5	14.8
18.2	4.1
24.8	1.3
33.0	0.9

[a]Four exponentials were needed to fully capture the decay.

To highlight the morphology of NaPy aggregates, a photograph of NaPy single crystals is shown in Figure 2a.

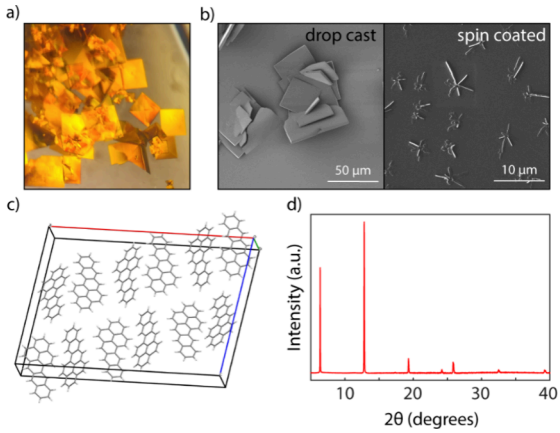

Figure 2. a) Photograph of NaPy single crystals. b) SEM-SE micrographs of a drop cast and spin coated NaPy thin film. c) NaPy single crystal structure obtained by single crystal X-ray diffraction highlighting the herringbone pattering in the P21/c space group. d) Room temperature NaPy thin film powder X-ray diffraction pattern.

Scanning electron microscopy (SEM) secondary electron (SE) images of a NaPy thin film drop cast (left) and spin coated (right) from the 33.0 mM stock solution are shown in Figure 2b. For the spin-coated film, initial nucleation is followed by two-dimensional ribbon-type growth feathering out from the nucleation site. Increasing the growth time by slow evaporation of the solvent by drop casting results in square platelet-like growth, highlighting that crystal growth occurs in a preferential direction. To verify that the square platelets are not unique to drop casting, Figure S2 shows a different region of the spin-coated NaPy film showing both square platelets as well as the ribbons feathered out from the nucleation sites. Single crystal X-ray diffraction of the crystals shown in Figure 2a reveals a P21/c space group, and the unit cell is shown in Figure 2c (the full unit cell parameters are listed in Table S2). The powder X-ray diffraction (Figure 2d) of the thin films yields reflections that are not consistent with expected positions based on single crystal structure (SI Figure S2), which is either due to residual solvent inclusion or formation a different polymorph. Furthermore, the thin film is highly textured, with a d-spacing perpendicular to the film of $d(001)$ = 13.807(3) Å (at room temperature of 295 K). The precise crystal structure resulting in the powder pattern could not be solved due to the low

https://doi.org/10.1021/acs.jpcc.4c05675
J. Phys. Chem. C 2024, 128, 19248−19259

number of observed reflections resulting from preferred orientations.

To understand the underlying properties of the different emissive states present in NaPy based on the molecular concentration, in the following, we study the temperature-dependent emission properties of the NaPy/PMMA thin films. Figure 3 depicts the change in the emission properties between 300 and 50 K for the 1.7 mM NaPy/PMMA thin film.

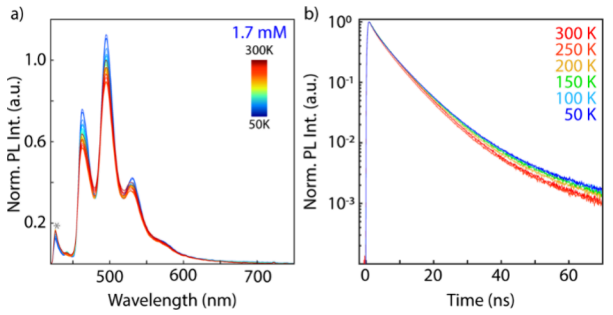

Figure 3. a) Temperature-dependent fluorescence spectra for the 1.7 mM NaPy/PMMA thin film collected under 405 nm excitation (3 W cm^{-2}). The spectra are normalized to the 300 K spectrum, and spectra were in 10 K increments. b) Emission decays for the 1.7 mM NaPy/PMMA film collected at selected temperatures collected under 405 nm pulsed excitation (1 MHz, 67 mW cm^{-2}).

After an initial minor drop in quantum yield up to 240 K, the quantum yield increases by 17% over the initial value when the lowest temperature of 50 K is reached. No changes or shifts in the spectral features are observed other than a slight narrowing of the vibronic features. The fluorescence lifetimes are fit to a triexponential function, and the calculated amplitude-averaged weighted lifetimes concurrently slightly increase from 5.7 to 5.9 ns (Table 2, Table S3). This minor increase in quantum

Table 2. Amplitude-Weighted Average Lifetimes for the 1.7 mM NaPy/PMMA Thin Film Based on a Triexponential Fit

Temp/K	τ_{ave}/ns
300	5.7
250	5.4
200	5.8
150	5.9
100	5.8
50	5.9

yield and lifetime is easily explained by the high inherent quantum yield of NaPy. We measure a quantum yield of 80% in solution. The relative quantum yield of the 1.7 mM NaPy/PMMA thin film is calculated at only 25%, however, slight H-type aggregation, solid-state outcoupling losses and scattering losses in the PMMA matrix are not considered in this calculation. However, to first approximation, we expect the isolated NaPy molecules in the PMMA matrix to behave similar to NaPy molecules in solution and possess an intrinsic high quantum yield. Therefore, the 17% increase in relative emission intensity would result in a near-unity quantum yield.

Next, the temperature-dependent optical properties of the 8.3 mM NaPy/PMMA thin film are investigated (Figure 4). The temperature-dependent emission spectra are highlight in Figure 4a. Here, the emission spectrum can be reconstructed by linear combination of two basis spectra corresponding to a

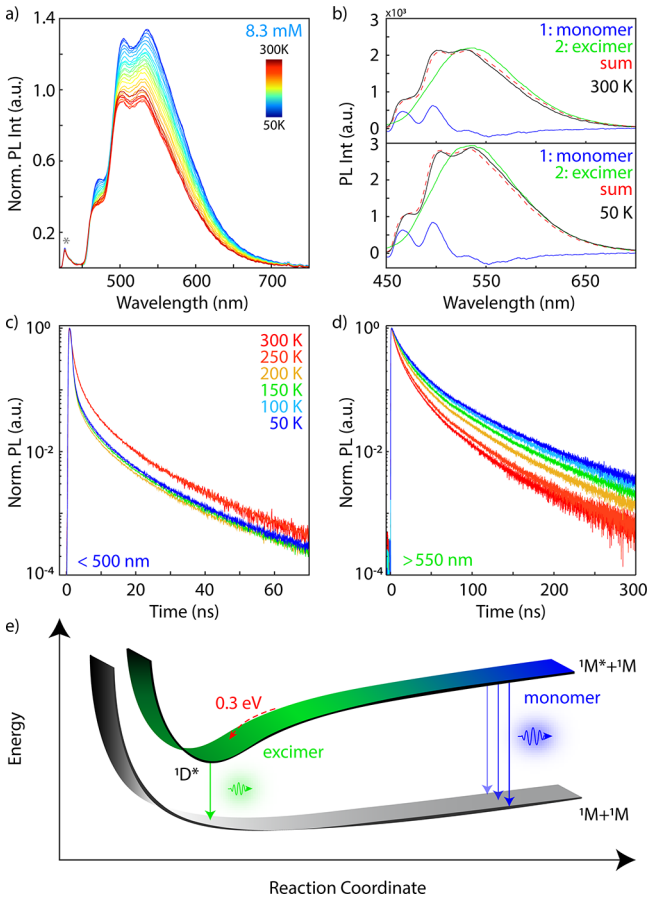

Figure 4. a) Temperature-dependent emission spectra for the 8.3 mM NaPy/PMMA thin film collected under 405 nm excitation (3 W cm^{-2}), normalized to the 300 K spectrum collected in 10 K increments. b) Spectral reconstruction of the 300 K (top) and 50 K (bottom) 8.3 mM NaPy/PMMA film from monomer-like (blue) and excimer-like (green) basis spectra (bottom). Fluorescence decays for the 8.3 mM NaPy/PMMA split into the c) monomer-like region (<500 nm) and d) excimer-like region (>550 nm) collected at selected temperatures. All decays were collected under 405 nm pulsed excitation (1 MHz, 67 mW cm^{-2}). e) Schematic energy diagram of the excimer formation.

monomer-like emission spectrum (Figure 4b, blue trace) which is slightly red-shifted with respect to the isolated monomer due to increased intermolecular coupling and a broad excimeric emission line shape (Figure 4b, green trace).

Strong changes in the spectral shape with decreasing temperature are expected if the excimer and monomer states are coupled and in thermal equilibrium, i.e., the excimer is formed through a thermally activated process over an activation barrier, as lowering the temperature reduces the available ambient thermal energy. Hence, a thermal activation barrier for excimer formation would shift the equilibrium to a higher population of monomer emission at lower temperature. In addition, any coupling between the states would favor emission from the excimer at low temperatures. However, as shown in Figure 4a, the spectral shape does not greatly change with temperature, mainly a sharpening of the vibronic features and an increase in intensity on the lower energy side of the emission is observed. Since the ratio of monomer to excimer emission does not change significantly, we conclude that there is no appreciable thermal activation barrier for excimer formation (Figure 4e). In addition, as a direct result of the

https://doi.org/10.1021/acs.jpcc.4c05675
J. Phys. Chem. C 2024, 128, 19248−19259

lack of change of the spectral shape, the data suggests that the populations of monomer and excimer are not directly coupled indicating that both isolated molecules and excimers are present in the fabricated sample.

However, the overall fluorescence intensity increase is much higher than previously observed for the monomer-like sample: 46%, which can be attributed to suppression of nonradiative decay pathways. To separate the dynamics two emissive states, we show the recombination dynamics for wavelengths <500 nm (monomer dominated) and >550 nm (excimer dominated) in Figure 4 c,d. In contrast to the emission lifetime for the monomer-like emission shown in Figure 3 for the 1.7 mM NaPy/PMMA film, here, there is an addition early time component for the dynamics <500 nm which can be attributed to intermolecular energy transfer. As observed previously for the 1.7 mM NaPy/PMMA sample, no distinct changes are observed for the monomer emission lifetime with temperature (the slightly longer lifetime of 250−300 K can be attributed to a higher fraction of overlapping excimer emission). However, the excimeric emission lifetime increases monotonically from 12.9 to 24.9 ns (Table 3, Table S4).

Table 3. Amplitude-Weighted Average Lifetimes for the Excimer-like Feature (>550 nm) for the 8.3 mM NaPy/PMMA Thin Film Based on a Triexponential Fit

Temp/K	τ_{ave}/ns
300	12.9
250	14.3
200	18.3
150	21.0
100	23.5
50	24.9

Similar behavior is observed in the 16.5 mM NaPy/PMMA sample, which shows only excimer-type emission at all temperatures between 300 K and 50K. As the temperature decreases, the quantum yield increases by 38% and a simultaneous increase in the amplitude-weighted average emission lifetime from 10.6 to 18.3 ns (Figure 5 a,b, Table 4, Table S5) is observed. No noticeable shift in the emission wavelength is observed with decreasing temperature. However, the lower energy side of the peak increases in relative intensity indicating that lower-energy excimers are favored at lower temperatures. The highly multiexponential (or stretched exponential) nature of the decay is unsurprising due to the vast parameter space of local molecular arrangements possible in these inhomogeneous thin films.

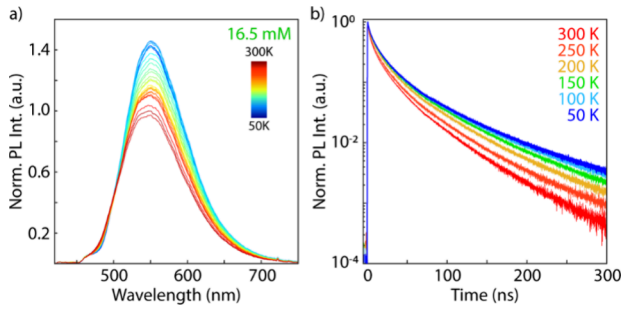

Figure 5. a) Temperature-dependent fluorescence spectra for the 16.5 mM NaPy/PMMA thin film collected under 405 nm excitation (3 W cm^{-2}), normalized to the 300 K spectra collected in 10 K increments. b) Emission decays for 16.5 mM NaPy/PMMA film collected at selected temperatures under 405 nm pulsed excitation (1 MHz, 67 mW cm^{-2}).

Table 4. Amplitude-Weighted Average Lifetimes for the 16.5 mM NaPy/PMMA Thin Film Based on a Quadruple Exponential Fit and the Fitting Parameters for a Stretched Exponential Fit $I(t) = A\exp(-(t/\tau)^c)$

Temp/K	quadruple exponential	stretched exponential	
	τ_{ave}/ns	τ/ns	c
300	10.6	4.0	0.47
250	12.3	4.8	0.47
200	14.9	6.4	0.49
150	16.7	7.2	0.50
100	17.7	7.4	0.50
50	18.3	7.5	0.49

The temperature dependence of the fluorescence of the 18.2 mM NaPy/PMMA film is shown in Figure 6a. In contrast to the 16.5 mM NaPy/PMMA sample (Figure 5) which showed emission only from the excimer state, different spectral features are observed despite the minor increase in concentration: a slight amount of monomer-related emission below 520 nm and emission corresponding to the aggregate structure at ∼520 nm. Initially, a continuous bathochromic shift of the aggregate emission is observed with decreasing temperature, as well as an enhancement of the fluorescence intensity. Simultaneously, the shoulder at ∼560 nm increases in intensity and becomes the dominant emission feature below ∼100 K, where a clear change in emission wavelength is observed with a corresponding line width broadening, indicating that the underlying emissive state is changing. An observation reminiscent of the dull state reported by Schmidt and co-workers for tetracene.[58] In agreement with the increased quantum yield upon cooling (∼4-fold relative intensity increase), the amplitude-weighted average fluorescence lifetime increases from 1.3 ns at 300 K to 4.9 ns at 50K (Figure 6b, Table 5, Table S6). Noteworthy is that the overall shape of the decay dynamics is different at 50 K, which is agreement with the previously mentioned change in dominant emissive state.

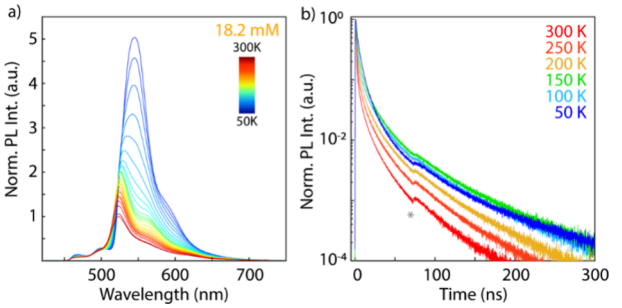

Figure 6. a) Temperature-dependent emission spectra for the 18.2 mM NaPy/PMMA thin film collected under 405 nm excitation (3 W cm^{-2}), normalized to the 300 K spectra collected in 10 K increments. b) Fluorescence decays for the 18.2 mM NaPy/PMMA film collected at selected temperatures under 405 nm pulsed excitation (1 MHz, 67 mW cm^{-2}). Asterisk denotes instrumental artifact.

Further increasing the NaPy concentration to 24.8 mM results in the expected aggregate emission at 520 nm and the emergence of an additional emissive feature at 620 nm (Figure 7a)—the feature we have previously observed to be highly

https://doi.org/10.1021/acs.jpcc.4c05675
J. Phys. Chem. C 2024, 128, 19248−19259

Table 5. Amplitude-Weighted Average Lifetimes for the 18.2 mM NaPy/PMMA Thin Film Based on a Triexponential Fit

Temp/K	τ_{ave}/ns
300	1.3
250	1.7
200	2.3
150	3.0
100	4.0
50	4.9

Table 6. Amplitude-Weighted Average Lifetimes for the 24.8 mM NaPy/PMMA Thin Film Based on Triexponential Fits at Temperatures between 300 and 50 K

Temp/K	τ_{ave}/ns 550/40 nm BP	τ_{ave}/ns 635/10 nm BP
300	1.1	5.7
250	1.3	6.7
200	1.8	8.3
150	2.3	9.3
100	2.8	10.5
50	4.8	10.1

TTA-UC active contrary to the higher energy state.[28] Due to the fact that this feature has not been present in any of the other thin films which are all made from the same stock solution (vide infra), we can rule out contamination of NaPy to be the underlying cause of this red-shifted emission.

With decreasing temperature, the high-energy emission at 520 nm again initially increases in quantum yield and shifts to lower energies. Simultaneously, the emission shoulder at ∼560 nm clearly increases in intensity with reducing temperature, while moderately shifting to higher energies (compare Figure S3), leading to an overall 7-fold increase in the integrated emission intensity.

The red-shifted feature at 620 nm appears to disappear with decreasing temperature, possibly indicating a thermally activated population pathway, or it is simply dwarfed by the overwhelming intensity of the overlapping emission. The fluorescence decay dynamics for the two features are different at room temperature, indicating that the emission stems from two distinct recombination pathways (Figure 7b,c) and not from the same state. The fluorescence lifetime of the high energy feature (isolated using a 550/40 center/width nm bandpass (BP) filter) strongly changes from an amplitude-weighted average lifetime of 1.1 ns at 300 K to 4.8 ns at 50 K. In contrast, the lifetime of the red-shifted feature (taken with a 635/10 nm BP filter) only changes from 5.7 ns at 300 K to 10.1 ns at 50 K (Table 6, Table S7). This minor change should be taken with a grain of salt, some contribution of the underlying dominant, blue-shifted emissive feature is not unexpected.

Lastly, we show the temperature dependence of the 33.0 mM NaPy sample (Figure 8), which is spin-coated directly from the stock solution. Very similar to the previous 24.8 mM NaPy/PMMA film, the peak emission redshifts and increases 9-fold in intensity with decreasing temperature (Figure 8a). Again, this is the result of an initial redshift and intensity increase of the peak at 520 nm, followed by a strong increase of emission intensity at 560 nm. A close look at the rise time of the time-resolved emission supports a change in the emissive state: the peak emission is delayed by ∼0.5 ns, indicating addition processes occurring prior to emission of a photon (Figure S5), rather than direct excitation of the emissive state.

No shift in the emission wavelength for the feature at 620 nm is found, indicating no temperature dependence of the exciton localization—attributed to emission from a localized state. The normalized temperature-dependent absorption of the 33.0 mM NaPy thin film is shown in Figure 8b, where only a sharpening of the absorption features is found. No absorption feature relating to the emission at 620 nm can be observed, indicating that this additional emissive state at 620 nm is present only in the excited state. The fluorescence lifetime increases for the high energy emission from 0.5 ns at 300 K to 3.6 ns at 100 K and then reduces to 3.0 ns at 50 K, while the lifetime of the lower energy feature stays nearly constant with an initial monoexponential decay of ∼8.3 ns (Figure 8c,d, Table 7, Table S8). The observed change in fluorescence decay dynamics at 550/40 nm is in agreement with the change in the dominant emissive feature seen in the steady-state emission. The constant fluorescence lifetime at 635/10 nm indicates that the feature at 620 nm remains the dominant emissive state at all temperatures and that it has no significant temperature-dependence of its recombination dynamics.

To ensure that the shift in the emission wavelength or dominant emissive feature is not caused by a change in the crystal structure of the NaPy, i.e., a phase transition, the temperature-dependent powder X-ray diffraction of NaPy is shown in Figure 8e. No additional reflections are observed as the temperature changes, only a shift of the reflections to higher angles 2θ as the temperature is decreased, corresponding to a lattice contraction. Based on the change in d-spacing

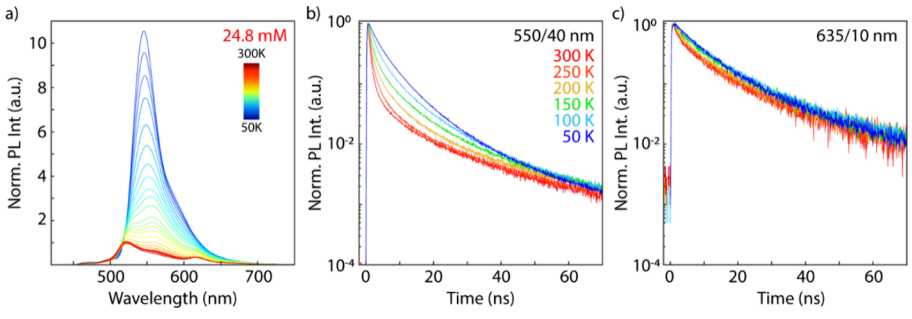

Figure 7. Temperature-dependent emission spectra for the 24.8 mM NaPy/PMMA thin film collected under 405 nm excitation (3 W cm^{-2}), normalized to the 300 K spectrum collected in 10 K increments. Fluorescence decays for the 24.8 mM NaPy/PMMA film collected under 405 nm pulsed excitation (1 MHz, 67 mW cm^{-2}) with a 550/40 nm BP filter (b) and 635/10 nm BP filter (c) at selected temperatures.

https://doi.org/10.1021/acs.jpcc.4c05675
J. Phys. Chem. C 2024, 128, 19248−19259

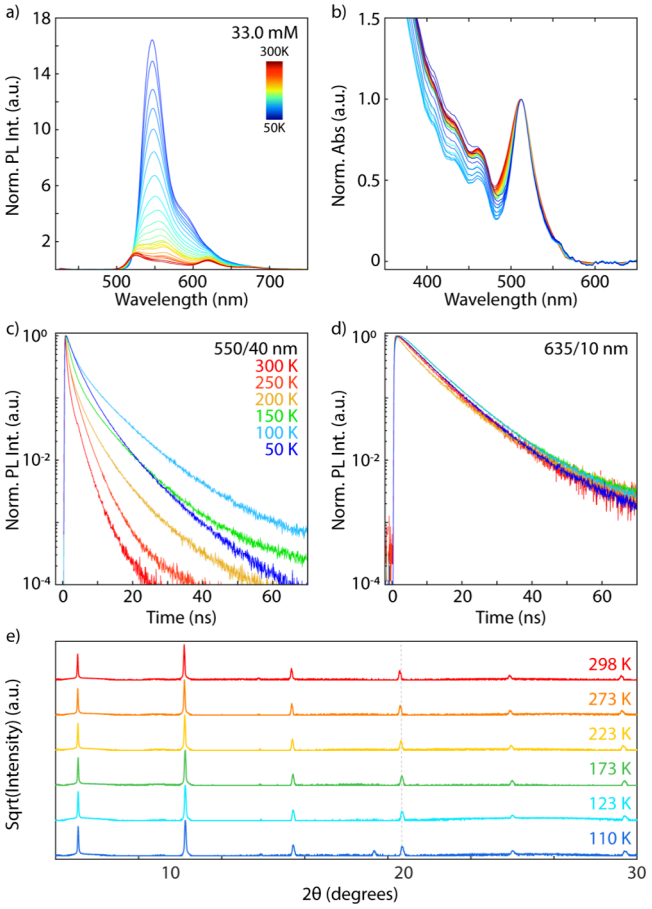

Figure 8. a) Temperature-dependent fluorescence spectra for the 33.0 mM NaPy/PMMA thin film collected under 405 nm excitation (3 W cm^{-2}), normalized to the 300 K spectrum collected in 10 K increments. b) Normalized temperature-dependent absorbance spectra for the 33.0 mM NaPy/PMMA thin film collected every 10 K. Corresponding fluorescence decays collected under 405 nm pulsed excitation (1 MHz, 67 mW cm^{-2}) with a 550/40 nm BP filter (c) and 635/10 nm BP filter (d) at selected temperatures. e) Normalized NaPy temperature-dependent thin film diffraction patterns collected at selected temperatures. The dashed gray line is included as a guide to the eye.

Table 7. Extracted Lifetimes for the 33.0 mM NaPy/PMMA Temperature-Dependent Fluorescence Decays Based a Triexponential Fit[a] and a Monoexponential Fit[b]

Temp/K	τ_{ave}/ns 550/40 nm BP	τ_{ave}/ns 635/10 nm BP
300	0.5	8.2
250	1.0	8.1
200	1.1	8.3
150	2.1	8.5
100	3.6	8.4
50	3.0	8.2

[a]550/40 nm BP. [b]635/10 nm BP.

with temperature, we extract a thermal expansion coefficient of approximately 4.24 × 10^{-4} Å/K and a relative expansion coefficient of approximately 30.69 × 10^{-6} K^{-1} between 110 and 300 K (compare Figure S6 and Table S9).

These results give rise to three unanswered questions in the photophysical investigation of NaPy: (i) what is the type of aggregate present in NaPy? (ii) What is causing the additional red-shifted feature at 620 nm at room temperature? And (iii) What is the nature of the dominant emissive state at low temperatures?

While previous reports have attributed the aggregate type of NaPy to a J-aggregate based on the red-shifted absorption spectrum with respect to the monomeric spectrum, our results are at odds with the properties of a true J-aggregate. The redistribution of the oscillator strength resulting in a redshift of the absorption spectrum rules out the formation of an H-type aggregate.[34,43] Based on the unchanged absorption spectrum with decreasing temperature (Figure 8b), we conclude that the aggregate is best represented by the I-aggregate described by Caram and co-workers:[34] both long-range J- and short-range H-type coupling are present, however, the long-range J-type coupling is more dominant and the bright state is at a local minimum of the density of states.[34]

The next question we will address is what the additional red-shifted emissive feature at 620 nm observed at room temperature is. We rule out the coupled triplet pair state ^{1}(TT) generated either directly by singlet fission or via subsequent TTA,[59,60] as the emission is significantly lowered with respect to the singlet state (~0.4 eV), making endothermic TTA-UC to the high-energy state unlikely.[28] However, we do observe upconversion to this state, and subsequent emission, albeit weakly. Furthermore, such a low ^{1}(TT) state energy with respect to S_1 is at odds with previous reports of both singlet fission and TTA-UC in NaPy, indicating the ^{1}(TT) state should be similar in energy as S_1.[28,31]

Clearly, the feature at 620 nm is a strongly coupled state, resulting in a strong bathochromic shift of the emission with respect to the singlet state. However, the corresponding absorption spectrum does not indicate an additional optical transition present for the ground state. Hence, we can conclude that similar to the excimer observed, this is a purely excited state phenomenon. Excimeric-type emission is also in agreement with the relatively long-lived fluorescence lifetime. However, excimer emission is generally broad and featureless, hence, not in complete agreement with the observed emission spectrum. However, considering an ordered, strongly J-coupled dimer, where the emission is delocalized over exactly two molecules, vibronic structure has been observed.[54,55] Another indication that this emission does not stem from a delocalized state is found in the temperature-dependent properties of its emission. In contrast to the main aggregate emission at 520 nm, this red-shifted feature at 620 nm does not shift with decreasing temperature, indicating that the wave function delocalization is not dependent on temperature. Hence, we suggest that this additional feature is caused by a strongly coupled localized J-dimer or a J-type excimer, which can be thought of as a local structural defect or trap site which results in strong interactions between the molecules. Since this feature is only present in films which are concentrated enough to show aggregate emission, we conclude that it cannot be populated directly through the excimer state, rather must be populated via another pathway: either directly from the aggregate S_1 state or through the ^{1}(TT) state prior to singlet fission.

This leads us to the discussion of the final mystery of NaPy—what is the underlying nature of the additional emission dominating the spectrum at low temperatures? Clearly, based on the temperature-dependent X-ray diffraction, no substantial change in crystal structure is observed between

https://doi.org/10.1021/acs.jpcc.4c05675
J. Phys. Chem. C 2024, 128, 19248−19259

300−110 K. Furthermore, the lack of changes in the absorption spectrum emphasizes that only the emissive state is changed, not the fundamental allowed optical transitions. Hence, our results indicate that multiple emissive states are present that are accessible within $\sim k_B T$. At room temperature, the aggregate feature relaxes either directly to the ground state or relaxes through the excimer or J-dimer states (Figure 9a), or

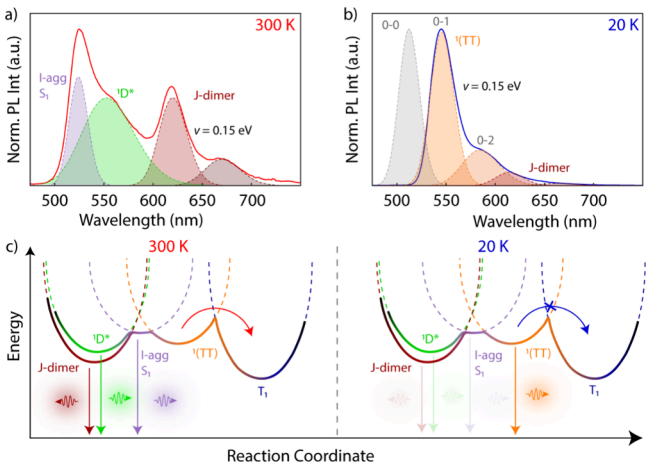

Figure 9. a) Emission spectra for the NaPy thin film (33.0 mM) at 300 and b) at 20 K with the Gaussian fits correlated to the I-aggregate emission, excimer, J-dimer and ^{1}(TT) state overlaid. The identities of the underlying features are labeled for clarity, as well as the vibronic spacing when present. The extrapolated ^{1}(TT) 0−0 vibronic feature is shown (not to scale) in gray at 20 K. c) Schematic of the NaPy energetic landscape. At low temperatures, direct emission from the triplet pair state ^{1}(TT) is observed, while at room temperature nonemissive uncorrelated triplets are formed.

undergoes singlet fission to generate triplet states as suggested by previous reports.[31] However, at lower temperatures, another emissive state becomes relevant (Figure 9b), which at higher temperatures can either thermalize back to the aggregate S_1 state, or relax through other nonradiative pathways. A simple schematic of the relaxation pathways is shown in Figure 9c. Considering previous reports of singlet fission in NaPy, and similar low-temperature spectra observed for the parent molecule tetracene which have been attributed to either a "dull state" with multiexciton character,[58] or direct emission from the ^{1}(TT) state,[59,61] we suggest that the low-temperature emission is dominated is by direct emission from the ^{1}(TT) state, which is allowed due to Herzberg−Teller coupling.[61] At room temperature, there is sufficient ambient energy available to form free triplet states from the correlated triplet pair state, hence, no emission is observed from this state. At low temperatures on the other hand, there is not sufficient ambient thermal energy present to overcome the activation barrier ΔE_a to split the correlated triplet pair state ^{1}(TT) into two uncorrelated triplet states T_1.[59,61]

$$^1(\mathrm{TT}) \xrightarrow{\Delta E_a} T_1 + T_1 \tag{5}$$

Assuming T_1 = 1.23 eV as calculated previously,[31] the energy of two uncorrelated triplet states is $E(T_1+T_1)$ = 2.46 eV. The 0−0 transition of the ^{1}(TT) state is commonly not observed or only observed with significantly suppressed intensity in ordered structures due to the Herzberg−Teller coupling mechanism allowing emission to occur.[59,61] Hence, the energy of the state can be extrapolated by adding the energy of the vibronic progression $\hbar\omega$ to the observed "0−1" emission feature. In agreement with an energy barrier ΔE_a close to the ambient thermal energy $k_B T \approx 25$ meV, since emission from the ^{1}(TT) rapidly emerges as we cool below 250 K, we extrapolate the energy of the ^{1}(TT) state: $E(^1(\mathrm{TT}))$ = 2.42 eV.

CONCLUSIONS

In summary, our results indicate that NaPy has several different emissive states dependent on the local environment of the NaPy molecules and the temperature. At low concentrations, we observe monomer-like emission. With increasing NaPy concentration, i.e., increasing intermolecular interactions, excimeric emission appears. Upon further increase in concentration, ordered I-aggregates are formed, and an additional increase in concentration results in emission from J-dimers.

The room temperature optical properties are summarized in Figure 9a, which shows the spectral composition of the solid-state NaPy spectrum based on the individual emissive states present: the I-aggregate, excimer and J-dimer. At low temperatures, the dominant emission feature changes, and the primary emission feature is attributed to emission from the bound ^{1}(TT) state based on the similarity with the low-temperature emission of the tetracene ^{1}(TT) state.[58,59]

Lastly, we discuss these results in context of our previous results on perovskite-sensitized upconversion in NaPy.[19,28] Our results indicated that there was a change in the primary emissive feature, depending upon whether NaPy was directly excited or emission was the result of charge injection from a lead halide perovskite to the triplet state of the NaPy molecule resulting in TTA-UC.[28] Several underlying reasons are possible. We had previously hypothesized that the lowered energy of this emissive state results in energetically favored upconversion, with no detrimental effects of possible singlet fission due to an energy mismatch, while the higher energy I-aggregate state may only be accessible through thermal excitation from the ^{1}(TT) state or through entropic effects. However, considering the strongly coupled nature of the J-dimer and the unfavorable singlet fission from this feature, the J-dimers may act as hotspots for preferential triplet−triplet annihilation−strong coupling could result in a favorable annihilation process. The J-dimer state may also be able to act as a triplet trap, facilitating the upconversion process. Another possibility may be a more favorable coupling between the ^{1}(TT) state and the state leading to emission at 620 nm, leading to preferential conversion of the ^{1}(TT) state to the J-dimer. Additional detailed spectroscopic studies based on transient absorption will be required to fully entangle the existing relaxation pathways and time scales in NaPy.

In conclusion, we have investigated the optical properties of NaPy as a function of temperature and local environment. We find that intermolecular interactions tune the emission of NaPy from its molecular emission spectrum through an excimer emission to an I-aggregate emission. J-dimer emission is observed in the bulk, and we hypothesize that the strongly coupled nature of this localized state facilitates photon upconversion in this molecule. At low temperatures an additional feature dominates the emission spectrum, which we attribute to emission from the correlated triplet pair state ^{1}(TT).

https://doi.org/10.1021/acs.jpcc.4c05675
J. Phys. Chem. C 2024, 128, 19248−19259

■ ASSOCIATED CONTENT

Data Availability Statement

Raw data files are available at DOI: 10.17605/OSF.IO/S276H.

Supporting Information

The Supporting Information is available free of charge at https://pubs.acs.org/doi/10.1021/acs.jpcc.4c05675.

Supporting figures containing additional optical spectroscopy, XRD pattern comparisons, SEM-SE micrographs, and thermal expansion coefficient fits; Supporting tables listing the fit parameters for the fluorescence decays, single crystal unit cell parameters, and the *d*-spacings at the different temperatures (PDF)

■ AUTHOR INFORMATION

Corresponding Author

Lea Nienhaus − *Department of Chemistry, Rice University, Houston, Texas 77005, United States; Department of Physics and Astronomy and Rice Advanced Materials Institute, Rice University, Houston, Texas 77005, United States;* orcid.org/0000-0003-1412-412X; Email: nienhaus@rice.edu

Authors

Colette M. Sullivan − *Department of Chemistry, Rice University, Houston, Texas 77005, United States;* orcid.org/0000-0001-8660-4056

Adrienn M. Szucs − *Center for Rare Earths, Critical Minerals, Industrial Byproducts National High Magnetic Field Laboratory Florida State University, Tallahassee, Florida 32310, United States;* orcid.org/0000-0001-8218-9174

Theo Siegrist − *Center for Rare Earths, Critical Minerals, Industrial Byproducts National High Magnetic Field Laboratory Florida State University, Tallahassee, Florida 32310, United States; FAMU-FSU College of Engineering, Tallahassee, Florida 32310, United States;* orcid.org/0000-0001-5368-1442

Complete contact information is available at: https://pubs.acs.org/10.1021/acs.jpcc.4c05675

Notes

The authors declare no competing financial interest.

■ ACKNOWLEDGMENTS

C.M.S. and L.N. acknowledge funding by the National Science Foundation under grant no. DMR-2237977 and support by the Camille and Henry Dreyfus Foundation in form of a Teacher-Scholar Award (TC-23-050). T.S. acknowledges funding from the National Science Foundation under grant no. DMR-2219906. Part of this work was performed at the Center for Rare Earths, Critical Minerals, and Industrial Byproducts of the National High Magnetic Field Laboratory, Florida State University, supported by the State of Florida through Contract #0000071627. The National High Magnetic Field Laboratory is supported by the National Science Foundation under Grants DMR-1644779 and DMR-2128556, as well as the State of Florida.

■ REFERENCES

(1) Hu, M.; Belliveau, E.; Wu, Y.; Narayanan, P.; Feng, D.; Hamid, R.; Murrietta, N.; Ahmed, G. H.; Kats, M. A.; Congreve, D. N. Bulk Heterojunction Upconversion Thin Films Fabricated via One-Step Solution Deposition. *ACS Nano* **2023**, *17* (22), 22642−22655.

(2) Alves, J.; Feng, J.; Nienhaus, L.; Schmidt, T. W. Challenges, Progress and Prospects in Solid State Triplet Fusion Upconversion. *J. Mater. Chem. C* **2022**, *10* (20), 7783−7798.

(3) Amemori, S.; Sasaki, Y.; Yanai, N.; Kimizuka, N. Near-Infrared-to-Visible Photon Upconversion Sensitized by a Metal Complex with Spin-Forbidden yet Strong S_0-T_1 Absorption. *J. Am. Chem. Soc.* **2016**, *138* (28), 8702−8705.

(4) Mase, K.; Okumura, K.; Yanai, N.; Kimizuka, N. Triplet Sensitization by Perovskite Nanocrystals for Photon Upconversion. *Chem. Commun.* **2017**, *53* (59), 8261−8264.

(5) Huang, Z.; Xu, Z.; Mahboub, M.; Li, X.; Taylor, J. W.; Harman, W. H.; Lian, T.; Tang, M. L. PbS/CdS Core-Shell Quantum Dots Suppress Charge Transfer and Enhance Triplet Transfer. *Angew. Chem.* **2017**, *129* (52), 16810−16814.

(6) Luo, X.; Han, Y.; Chen, Z.; Li, Y.; Liang, G.; Liu, X.; Ding, T.; Nie, C.; Wang, M.; Castellano, F. N.; et al. Mechanisms of Triplet Energy Transfer across the Inorganic Nanocrystal/Organic Molecule Interface. *Nat. Commun.* **2020**, *11* (1), 28.

(7) Garakyaraghi, S.; Mongin, C.; Granger, D. B.; Anthony, J. E.; Castellano, F. N. Delayed Molecular Triplet Generation from Energized Lead Sulfide Quantum Dots. *J. Phys. Chem. Lett.* **2017**, *8* (7), 1458−1463.

(8) Gholizadeh, E. M.; Prasad, S. K. K.; Teh, Z. L.; Ishwara, T.; Norman, S.; Petty, A. J.; Cole, J. H.; Cheong, S.; Tilley, R. D.; Anthony, J. E.; et al. Photochemical Upconversion of Near-Infrared Light from below the Silicon Bandgap. *Nat. Photonics* **2020**, *14* (9), 585−590.

(9) Cheng, Y. Y.; Khoury, T.; Clady, R. G. C. R.; Tayebjee, M. J. Y.; Ekins-Daukes, N. J.; Crossley, M. J.; Schmidt, T. W. On the Efficiency Limit of Triplet-Triplet Annihilation for Photochemical Upconversion. *Phys. Chem. Chem. Phys.* **2010**, *12* (1), 66−71.

(10) Schmidt, T. W.; Castellano, F. N. Photochemical Upconversion: The Primacy of Kinetics. *J. Phys. Chem. Lett.* **2014**, *5* (22), 4062−4072.

(11) Han, Y.; Luo, X.; Lai, R.; Li, Y.; Liang, G.; Wu, K. Visible-Light-Driven Sensitization of Naphthalene Triplets Using Quantum-Confined CsPbBr3 Nanocrystals. *J. Phys. Chem. Lett.* **2019**, *10* (7), 1457−1463.

(12) He, S.; Luo, X.; Liu, X.; Li, Y.; Wu, K. Visible-to-Ultraviolet Upconversion Efficiency above 10% Sensitized by Quantum-Confined Perovskite Nanocrystals. *J. Phys. Chem. Lett.* **2019**, *10* (17), 5036−5040.

(13) Bender, J. A.; Raulerson, E. K.; Li, X.; Goldzak, T.; Xia, P.; Van Voorhis, T.; Tang, M. L.; Roberts, S. T. Surface States Mediate Triplet Energy Transfer in Nanocrystal-Acene Composite Systems. *J. Am. Chem. Soc.* **2018**, *140* (24), 7543−7553.

(14) Huang, Z.; Tang, M. L. Designing Transmitter Ligands That Mediate Energy Transfer between Semiconductor Nanocrystals and Molecules. *J. Am. Chem. Soc.* **2017**, *139* (28), 9412−9418.

(15) Sullivan, C. M.; Bieber, A. S.; Drozdick, H. K.; Moller, G.; Kuszynski, J. E.; VanOrman, Z. A.; Wieghold, S.; Strouse, G. F.; Nienhaus, L. Surface Doping Boosts Triplet Generation Yield in Perovskite-Sensitized Upconversion. *Adv. Opt. Mater.* **2023**, *11* (1), 2201921.

(16) Nienhaus, L.; Correa-Baena, J.-P.; Wieghold, S.; Einzinger, M.; Lin, T.-A.; Shulenberger, K. E.; Klein, N. D.; Wu, M.; Bulović, V.; Buonassisi, T.; et al. Triplet-Sensitization by Lead Halide Perovskite Thin Films for Near-Infrared-to-Visible Upconversion. *ACS Energy Lett.* **2019**, *4*, 888−895.

(17) Wang, L.; Yoo, J. J.; Lin, T.-A.; Perkinson, C. F.; Lu, Y.; Baldo, M. A.; Bawendi, M. G. Interfacial Trap-Assisted Triplet Generation in Lead Halide Perovskite Sensitized Solid-State Upconversion. *Adv. Mater.* **2021**, *33* (27), 2100854.

(18) Prashanthan, K.; Naydenov, B.; Lips, K.; Unger, E.; MacQueen, R. W. Interdependence of Photon Upconversion Performance and Antisolvent Processing in Thin-Film Halide Perovskite-Sensitized Triplet-Triplet Annihilators. *J. Chem. Phys.* **2020**, *153* (16), 164711.

(19) Wieghold, S.; Bieber, A. S.; VanOrman, Z. A.; Daley, L.; Leger, M.; Correa-Baena, J.-P.; Nienhaus, L. Triplet Sensitization by Lead

Halide Perovskite Thin Films for Efficient Solid-State Photon Upconversion at Subsolar Fluxes. *Matter* **2019**, *1*, 705−719.
(20) Nienhaus, L.; Wu, M.; Geva, N.; Shepherd, J. J.; Wilson, M. W. B.; Bulović, V.; Van Voorhis, T.; Baldo, M. A.; Bawendi, M. G. Speed Limit for Triplet-Exciton Transfer in Solid-State PbS Nanocrystal-Sensitized Photon Upconversion. *ACS Nano* **2017**, *11* (8), 7848−7857.
(21) Wu, M.; Congreve, D. N.; Wilson, M. W. B.; Jean, J.; Geva, N.; Welborn, M.; Van Voorhis, T.; Bulović, V.; Bawendi, M. G.; Baldo, M. A. Solid-State Infrared-to-Visible Upconversion Sensitized by Colloidal Nanocrystals. *Nat. Photonics* **2016**, *10* (1), 31−34.
(22) Wu, M.; Jean, J.; Bulović, V.; Baldo, M. A. Interference-Enhanced Infrared-to-Visible Upconversion in Solid-State Thin Films Sensitized by Colloidal Nanocrystals. *Appl. Phys. Lett.* **2017**, *110* (21), 211101.
(23) Wieghold, S.; Bieber, A. S.; VanOrman, Z. A.; Rodriguez, A.; Nienhaus, L. Is Disorder Beneficial in Perovskite-Sensitized Solid-State Upconversion? Role of DBP Doping in Rubrene. *J. Phys. Chem. C* **2020**, *124* (33), 18132−18140.
(24) Duan, J.; Liu, Y.; Zhang, Y.; Chen, Z.; Xu, X.; Ye, L.; Wang, Z.; Yang, Y.; Zhang, D.; Zhu, H. Efficient Solid-State Infrared-to-Visible Photon Upconversion on Atomically Thin Monolayer Semiconductors. *Sci. Adv.* **2022**, *8* (43), No. eabq4935.
(25) Radiunas, E.; Dapkevičius, M.; Raišys, S.; Juršėnas, S.; Jozeliūnaitė, A.; Javorskis, T.; Šinkevičiūtė, U.; Orentas, E.; Kazlauskas, K. Impact of T-Butyl Substitution in a Rubrene Emitter for Solid State NIR-to-Visible Photon Upconversion. *Phys. Chem. Chem. Phys.* **2020**, *22* (14), 7392−7403.
(26) Sullivan, C. M.; Nienhaus, L. Recharging Upconversion: Revealing Rubrene's Replacement. *Nanoscale* **2022**, *14* (46), 17254−17261.
(27) Sullivan, C. M.; Nienhaus, L. Generating Spin-Triplet States at the Bulk Perovskite/Organic Interface for Photon Upconversion. *Nanoscale* **2023**, *15* (3), 998−1013.
(28) Sullivan, C. M.; Nienhaus, L. Turning on TTA: Tuning the Energy Landscape by Intermolecular Coupling. *Chem. Mater.* **2024**, *36* (1), 417−424.
(29) France, C. B.; Parkinson, B. A. Chiral Morphologies and Interfacial Electronic Structure of Naphtho[2,3-a]Pyrene on Au(111). *Langmuir* **2004**, *20* (7), 2713−2719.
(30) France, C. B.; Parkinson, B. A. Naphtho[2,3-a]Pyrene Forms Chiral Domains on Au(111). *J. Am. Chem. Soc.* **2003**, *125* (42), 12712−12713.
(31) Aggarwal, N.; Patnaik, A. Dimeric Conformation Sensitive Electronic Excited States of Tetracene Congeners and Their Unconventional Non-Fluorescent Behaviour. *J. Chem. Sci.* **2019**, *131* (6), 52.
(32) Bae, Y. J.; Kang, G.; Malliakas, C. D.; Nelson, J. N.; Zhou, J.; Young, R. M.; Wu, Y.-L.; Van Duyne, R. P.; Schatz, G. C.; Wasielewski, M. R. Singlet Fission in 9,10-Bis(Phenylethynyl)-Anthracene Thin Films. *J. Am. Chem. Soc.* **2018**, *140* (45), 15140−15144.
(33) Charbr, M.; Williams, D. F. Singlet Exciton Trapping and Heterofission in Tetracene Doped Anthracene Crystals. *Chem. Phys. Lett.* **1977**, *49* (3), 599−603.
(34) Deshmukh, A. P.; Geue, N.; Bradbury, N. C.; Atallah, T. L.; Chuang, C.; Pengshung, M.; Cao, J.; Sletten, E. M.; Neuhauser, D.; Caram, J. R. Bridging the Gap between H- and J-Aggregates: Classification and Supramolecular Tunability for Excitonic Band Structures in Two-Dimensional Molecular Aggregates. *Chem. Phys. Rev.* **2022**, *3* (2), 021401.
(35) Lim, S.-H.; Bjorklund, T. G.; Spano, F. C.; Bardeen, C. J. Exciton Delocalization and Superradiance in Tetracene Thin Films and Nanoaggregates. *Phys. Rev. Lett.* **2004**, *92* (10), 107402.
(36) Lin, K.-Y.; Wang, Y.-J.; Chen, K.-L.; Ho, C.-Y.; Yang, C.-C.; Shen, J.-L.; Chiu, K.-C. Role of Molecular Conformations in Rubrene Polycrystalline Films Growth from Vacuum Deposition at Various Substrate Temperatures. *Sci. Rep.* **2017**, *7* (1), 40824.
(37) Greenwell, C.; Beran, G. J. O. Rubrene Untwisted: Common Density Functional Theory Calculations Overestimate Its Deviant Tendencies. *J. Mater. Chem. C* **2021**, *9* (8), 2848−2857.
(38) Mukherjee, T.; Sinha, S.; Mukherjee, M. Electronic Structure of Twisted and Planar Rubrene Molecules: A Density Functional Study. *Phys. Chem. Chem. Phys.* **2018**, *20* (27), 18623−18629.
(39) Volek, T. S.; Armstrong, Z. T.; Sowa, J. K.; Wilson, K. S.; Bohlmann Kunz, M.; Bera, K.; Koble, M.; Frontiera, R. R.; Rossky, P. J.; Zanni, M. T.; Roberts, S. T. Structural Disorder at the Edges of Rubrene Crystals Enhances Singlet Fission. *J. Phys. Chem. Lett.* **2023**, *14* (50), 11497−11505.
(40) JELLEY, E. E. Spectral Absorption and Fluorescence of Dyes in the Molecular State. *Nature* **1936**, *138* (3502), 1009−1010.
(41) McRae, E. G.; Kasha, M. Enhancement of Phosphorescence Ability upon Aggregation of Dye Molecules. *J. Chem. Phys.* **1958**, *28* (4), 721−722.
(42) Hochstrasser, R. M.; Kasha, M. APPLICATION OF THE EXCITON MODEL TO MONO-MOLECULAR LAMELLAR SYSTEMS. *Photochem. Photobiol.* **1964**, *3* (4), 317−331.
(43) Chuang, C.; Bennett, D. I. G.; Caram, J. R.; Aspuru-Guzik, A.; Bawendi, M. G.; Cao, J. Generalized Kasha's Model: T-Dependent Spectroscopy Reveals Short-Range Structures of 2D Excitonic Systems. *Chem.* **2019**, *5* (12), 3135−3150.
(44) Spano, F. C.; Silva, C. H- and J-Aggregate Behavior in Polymeric Semiconductors. *Annu. Rev. Phys. Chem.* **2014**, *65* (1), 477−500.
(45) Hestand, N. J.; Spano, F. C. Expanded Theory of H- and J-Molecular Aggregates: The Effects of Vibronic Coupling and Intermolecular Charge Transfer. *Chem. Rev.* **2018**, *118* (15), 7069−7163.
(46) Voigt, M.; Langner, A.; Schouwink, P.; Lupton, J. M.; Mahrt, R. F.; Sokolowski, M. Picosecond Time Resolved Photoluminescence Spectroscopy of a Tetracene Film on Highly Oriented Pyrolytic Graphite: Dynamical Relaxation, Trap Emission, and Superradiance. *J. Chem. Phys.* **2007**, *127* (11), 114705.
(47) Yamagata, H.; Spano, F. C. Interplay between Intrachain and Interchain Interactions in Semiconducting Polymer Assemblies: The HJ-Aggregate Model. *J. Chem. Phys.* **2012**, *136* (18), 184901.
(48) Spano, F. C. EXCITONS IN CONJUGATED OLIGOMER AGGREGATES, FILMS, AND CRYSTALS. *Annu. Rev. Phys. Chem.* **2006**, *57*, 217−243.
(49) Spano, F. C. Temperature-Dependent Emission in Disordered Herringbone Aggregates: Stacking Faults and Point Defects. *6th Int. Conf. Excit. Process. Condens. Matter EXCON 04* **2005**, *112* (1), 395−401.
(50) Hoche, J.; Schmitt, H.-C.; Humeniuk, A.; Fischer, I.; Mitrić, R.; Röhr, M. I. S. The Mechanism of Excimer Formation: An Experimental and Theoretical Study on the Pyrene Dimer. *Phys. Chem. Chem. Phys.* **2017**, *19* (36), 25002−25015.
(51) Dimitriev, O. P.; Piryatinski, Y. P.; Slominskii, Y. L. Excimer Emission in J-Aggregates. *J. Phys. Chem. Lett.* **2018**, *9* (9), 2138−2143.
(52) Cho, D. W.; Cho, D. W. Excimer and Exciplex Emissions of 1,8-Naphthalimides Caused by Aggregation in Extremely Polar or Nonpolar Solvents. *New J. Chem.* **2014**, *38* (6), 2233−2236.
(53) Abd-El-Aziz, A. S.; Abdelghani, A. A.; Wagner, B. D.; Abdelrehim, E. M. Aggregation Enhanced Excimer Emission (AEEE) with Efficient Blue Emission Based on Pyrene Dendrimers. *Polym. Chem.* **2016**, *7* (19), 3277−3299.
(54) Tian, D.; Qi, F.; Ma, H.; Wang, X.; Pan, Y.; Chen, R.; Shen, Z.; Liu, Z.; Huang, L.; Huang, W. Domino-like Multi-Emissions across Red and near Infrared from Solid-State 2-/2,6-Aryl Substituted BODIPY Dyes. *Nat. Commun.* **2018**, *9* (1), 2688.
(55) Musser, A. J.; Rajendran, S. K.; Georgiou, K.; Gai, L.; Grant, R. T.; Shen, Z.; Cavazzini, M.; Ruseckas, A.; Turnbull, G. A.; Samuel, I. D. W.; Clark, J.; Lidzey, D. G. Intermolecular States in Organic Dye Dispersions: Excimers vs. Aggregates. *J. Mater. Chem. C* **2017**, *5* (33), 8380−8389.

https://doi.org/10.1021/acs.jpcc.4c05675
J. Phys. Chem. C 2024, 128, 19248−19259

(56) Betteridge, P. W.; Carruthers, J. R.; Cooper, R. I.; Prout, K.; Watkin, D. J. It CRYSTALS Version 12: Software for Guided Crystal Structure Analysis. *J. Appl. Crystallogr.* **2003**, *36* (6), 1487.
(57) Deshmukh, A. P.; Koppel, D.; Chuang, C.; Cadena, D. M.; Cao, J.; Caram, J. R. Design Principles for Two-Dimensional Molecular Aggregates Using Kasha's Model: Tunable Photophysics in Near and Short-Wave Infrared. *J. Phys. Chem. C* **2019**, *123* (30), 18702−18710.
(58) Tayebjee, M. J. Y.; Clady, R. G. C. R.; Schmidt, T. W. The Exciton Dynamics in Tetracene Thin Films. *Phys. Chem. Chem. Phys.* **2013**, *15* (35), 14797−14805.
(59) Yong, C. K.; Musser, A. J.; Bayliss, S. L.; Lukman, S.; Tamura, H.; Bubnova, O.; Hallani, R. K.; Meneau, A.; Resel, R.; Maruyama, M.; Hotta, S.; Herz, L. M.; Beljonne, D.; Anthony, J. E.; Clark, J.; Sirringhaus, H. The Entangled Triplet Pair State in Acene and Heteroacene Materials. *Nat. Commun.* **2017**, *8* (1), 15953.
(60) Stern, H. L.; Cheminal, A.; Yost, S. R.; Broch, K.; Bayliss, S. L.; Chen, K.; Tabachnyk, M.; Thorley, K.; Greenham, N.; Hodgkiss, J. M.; et al. Vibronically Coherent Ultrafast Triplet-Pair Formation and Subsequent Thermally Activated Dissociation Control Efficient Endothermic Singlet Fission. *Nat. Chem.* **2017**, *9* (12), 1205−1212.
(61) Musser, A. J.; Clark, J. Triplet-Pair States in Organic Semiconductors. *Annu. Rev. Phys. Chem.* **2019**, *70*, 323−351.

https://doi.org/10.1021/acs.jpcc.4c05675
J. Phys. Chem. C 2024, 128, 19248−19259